Interplay between chiral charge density wave and superconductivity in kagome superconductors studied by self-consistent mean-field theory

Hong-Min Jiang,[1,2,*] Min Mao,[1] Zhi-Yong Miao,[1] Shun-Li Yu,[2,3,†] and Jian-Xin Li[2,3,‡]
[1]*School of Science, Zhejiang University of Science and Technology, Hangzhou 310023, China*
[2]*National Laboratory of Solid State Microstructures and Department of Physics, Nanjing University, Nanjing 210093, China*
[3]*Collaborative Innovation Center of Advanced Microstructures, Nanjing University, Nanjing 210093, China*

(Received 25 October 2023; revised 26 January 2024; accepted 1 March 2024; published 18 March 2024)

Inspired by the recent discovery of a successive evolutions of electronically ordered states in the vanadium-based kagome superconductors, we present a self-consistent theoretical analysis that treats the interactions responsible for the chiral charge order and superconductivity on an equal footing. It is revealed that the self-consistent theory captures the essential features of the successive temperature evolutions of the electronic states from the high-temperature "triple-Q" 2×2 charge-density-wave state to the nematic charge-density-wave phase, and finally to the low-temperature superconducting state coexisting with the nematic charge density wave. We provide a comprehensive explanation for the temperature evolutions of the charge ordered states and discuss the consequences of the intertwining of the superconductivity with the nematic charge density wave. Our findings not only account for the successive temperature evolutions of the ordered electronic states discovered in experiments but also provide a natural explanation for the twofold rotational symmetry observed in both the charge-density-wave and superconducting states. Moreover, the intertwining of the superconductivity with the nematic charge-density-wave order may also be an advisable candidate to reconcile the divergent or seemingly contradictory experimental outcomes regarding the superconducting properties.

DOI: 10.1103/PhysRevB.109.104512

I. INTRODUCTION

Kagome systems, with their geometrical frustration and nontrivial band topology, have long served as paradigmatic platforms for investigating exotic quantum phases of electronic matter, including spin liquid [1–9], superconductivity [10–15], various topological quantum phases [16–23], charge density wave (CDW) [16,24], spin-density wave [10], and bond density wave [12,13,25]. Of particular interest is the possible phases near the van Hove filling (VHF), especially the superconducting (SC) state, which overcomes the tendency to the density waves in the presence of a prefect nesting Fermi surface (FS) due to its intrinsic sublattice textures [10]. This special sublattice character of the Bloch state on the FS and its associated sublattice interference effect have an important influence on the interaction physics and play a crucial role in the potential for superconductivity and various density-wave instabilities [10–13,26]. These unique properties of the electron structure lead to the SC state being susceptible to competition from various other electronic instabilities. Understanding the superconductivity in such a kagome material that either avoids or even intertwines with these competing instabilities remains an unsettled issue.

The recent discovery of superconductivity in a family of compounds AV_3Sb_5 ($A = $ K, Rb, Cs), which share a common lattice structure with kagome net of vanadium atoms, has set off a new boom of research into superconductivity [27–76]. The appealing aspects of these compounds lie in that they incorporate many remarkable properties of the electron structure, such as VHF, FS nesting, and nontrivial band topology [27]. Numerous unique features of these materials have been unveiled both experimentally and theoretically. For instance, twofold van Hove singularities (VHSs) with opposite concavity have been observed near the Fermi level in angle-resolved photoemission spectroscopy (ARPES) experiments [49], and a recent parquet renormalization-group study revealed interesting orbital orders in the twofold-VHS framework [75].

Consistent with the fairly good FS nesting and proximity to the van Hove singularities, the system undergoes a "triple-Q" 2×2 CDW transition at temperature $T_{\mathrm{CDW}} \approx$ 78–104 K, with the in-plane wave vectors align with those connecting the VHSs [27,34,37,38,40,64,74]. While the neutron scattering [77] and muon spin spectroscopy [78] measurements have ruled out the possibility of long-range magnetic order in AV_3Sb_5, a significant anomalous Hall effect is still observed above the onset of the SC state in this 2×2 CDW phase [28,35], pointing to a time-reversal symmetry-breaking state originating from the charge degree of freedom [78]. Even if the notion of the time-reversal symmetry-breaking state has been further strengthened by the polar Kerr effect [79] and scanning tunneling microscopy (STM) experiment [34], conflicting results have also been reported by different groups [80,81], and the anomalous Hall effect could possibly be explained as well by skew

*monsoonjhm@sina.com
†slyu@nju.edu.cn
‡jxli@nju.edu.cn

scattering or a field-induced transition to a time-reversal symmetry-breaking phase [28]. Although the question of the time-reversal symmetry-breaking state is still unsettled in this field [63,82], there are an increasing amount of experimental evidence supporting that the CDW state has a 2×2 chiral flux order [34,52,63,74,79,83–86], i.e., the chiral flux phase (CFP) [87–89]. Furthermore, the muon-spin-relaxation technique observed a noticeable enhancement of the internal field width, which takes place just below the charge ordering temperature and persists into the SC state [74], suggesting an intertwining of time-reversal symmetry-breaking charge order with superconductivity.

Nevertheless, more recent experiments revealed that the high-temperature 2×2 CDW state does not directly border the low-temperature SC state. Instead, the high-temperature 2×2 CDW state is separated from the SC ground state by an intermediate-temperature regime with the twofold (C_2) rotational symmetry of electron state [57,62,90,91], the so-called electronic nematicity, in which there seems to exist a favored Q instead of the "triple-Q" to gain more condensation, resulting in the breakdown of the sixfold rotational symmetry to a twofold symmetry. The rotationally symmetry-breaking state is found to evolve at temperature T_{nem} beneath T_{CDW} [57,62,90,91] or directly from the normal state [92] and persist into the SC state, as evinced by transport [45] and STM measurements [37,62].

Apart from the exotic charge orders, the superconductivity in AV_3Sb_5 exhibits some unusual features as well. On the one hand, the SC pairings in these compounds are suggested to be of the s-wave type, supported by the appearance of the Hebel-Slichter coherence peak just below T_c in the nuclear magnetic resonance spectroscopy [41] and the nodeless SC gap in both the penetration depth measurements [44] and the ARPES experiment [93]. On the other hand, the indications of time-reversal symmetry breaking and the C_2 rotational symmetry discovered in the SC state [37,45,62,74,93], together with the nodal SC gap feature detected by some experiments [38–40,42], hint to an unconventional superconductivity.

Since the superconductivity occurs within the density wave ordered state, understanding the relationship between the CDW instability and superconductivity is a central issue in the study of AV_3Sb_5. Theoretical analysis has shown that a conventional fully gapped superconductivity is unable to open a gap on the domains of the CFP and results in the gapless edge modes in the SC state [94]. A more direct consideration of the impact of the chiral 2×2 CDW on the SC properties has revealed that a nodal SC gap feature shows up even if an on-site s-wave SC order parameter is included in the study [95]. However, there is still limited knowledge about the rotational-symmetry-breaking phase that straddles the SC ground state and the 2×2 CDW state in this class of kagome metals, particularly its origin, its role in the formation of the superconductivity, and its impact on the SC properties.

In this paper, we investigate the interplay between the CFP and superconductivity in a fully self-consistent theory, which self-consistently treats both the chiral CDW and the SC pairing orders on an equal footing. The calculated results catch the essential characteristics of the successive temperature evolutions of the electronically ordered states, starting from the high-temperature 2×2 "triple-Q" CFP (TCFP) to the nematic CFP (NCFP), and finally to the low-temperature SC state. Notably, the SC state emerges in the coexistence with the NCFP, by which the free energy in the coexisting phase is significantly lower than that in the pure SC state. The rotational symmetry-breaking transition of the CDW can be understood from a competitive scenario, in which the delicate competition between the doping deviation from the VHF and the thermal broadening of the FS determines the energetically favored state. In the coexisting phase of the s-wave SC pairing and the NCFP order, the density of states (DOS) exhibits a nodal gap feature manifesting as the V-shaped DOS along with the residual DOS near the Fermi energy. These results not only reproduce the successive temperature evolutions of the ordered electronic states observed in experiment but also provide a tentative explanation to the twofold rotational symmetry observed in both the CDW and SC states. Furthermore, the intertwining of the SC pairing with the NCFP order may also be an advisable candidate to reconcile the divergent or seemingly contradictory experimental outcomes concerning the SC properties.

The remainder of the paper is organized as follows: In Sec. II, we introduce the model Hamiltonian and carry out analytical calculations. In Sec. III, we present numerical calculations and discuss the results. In Sec. IV, we make a conclusion.

II. MODEL AND METHOD

It is generally considered that the scattering due to the FS nesting, especially the interscattering between three van Hove points with the nesting wave vectors $\mathbf{Q}_a = (-\pi, \sqrt{3}\pi)$, $\mathbf{Q}_b = (-\pi, -\sqrt{3}\pi)$, and $\mathbf{Q}_c = (2\pi, 0)$ shown in Fig. 1(b), is closely related to the CDW in AV_3Sb_5. Meanwhile, the VHF was also proposed to be crucial to the superconductivity in AV_3Sb_5. A single-orbital tight-binding model near the VHF produces the essential feature of the FS and the van Hove physics [10]. Therefore, to capture the main physics of the chiral CDW and its intertwining with the SC in AV_3Sb_5, we adopt a minimum single orbital model. We also note that the sixfold (C_6) symmetry is broken within the unit-cell of the 2×2 CDW state [57], without any additional reduction in translation symmetry. Thus, we choose the enlarged unit cell (EUC) with size $2\mathbf{a}_1 \times 2\mathbf{a}_2$, as indicated by the dashed lines in Fig. 1(a).

The single orbital model can be described by the following tight-binding Hamiltonian,

$$H_0 = -t \sum_{\langle \mathbf{ij} \rangle \alpha} c^\dagger_{\mathbf{i}\alpha} c_{\mathbf{j}\alpha} - \mu \sum_{\mathbf{i}\alpha} c^\dagger_{\mathbf{i}\alpha} c_{\mathbf{i}\alpha}, \tag{1}$$

where $c^\dagger_{\mathbf{i}\alpha}$ creates an electron with spin α on the site $\mathbf{r}_i$ of the kagome lattice and $\langle \mathbf{ij} \rangle$ denotes nearest-neighbors (NNs). t is the hopping integral between the NN sites, and μ stands for the chemical potential. Hereafter, we use t as an energy unit. The Hamiltonian H_0 can be written in the momentum space as,

$$H_0(\mathbf{k}) = \sum_{\mathbf{k}\alpha} \hat{\Psi}^\dagger_{\mathbf{k}\alpha} \hat{\mathcal{H}}^0_{\mathbf{k}} \hat{\Psi}_{\mathbf{k}\alpha}, \tag{2}$$

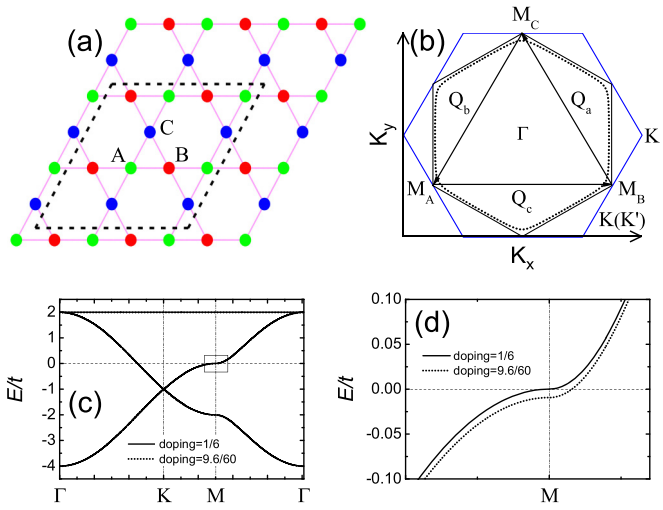

FIG. 1. (a) Structure of the kagome lattice, made out of three sublattices A (green dots), B (red dots), and C (blue dots). The dashed lines in the figure denote the enlarged unit cell in the 2×2 CDW state. (b) Fermi surface produced by the Hamiltonian $H_0(\mathbf{k})$ for the doping levels 1/6 (solid lines) and 9.6/60 (dotted lines), respectively. (c) Tight-binding dispersion along high-symmetry cuts for doping levels 1/6 (solid curve) and 9.6/60 (dotted curve). (Note that the solid and dotted curves are close to each other, so only one solid curve can be discerned in a large energy scale.) The dashed line denotes the Fermi level. (d) An enlarged view of the square box in panel (c).

with $\hat{\Psi}_{\mathbf{k}\alpha} = (c_{A\mathbf{k}\alpha}, c_{B\mathbf{k}\alpha}, c_{C\mathbf{k}\alpha})^T$ and

$$\hat{\mathcal{H}}^0_{\mathbf{k}} = \begin{pmatrix} -\mu & -2t\cos k_1 & -2t\cos k_2 \\ -2t\cos k_1 & -\mu & -2t\cos k_3 \\ -2t\cos k_2 & -2t\cos k_3 & -\mu \end{pmatrix}. \tag{3}$$

The index $m = A, B, C$ in $c_{mk\sigma}$ labels the three basis sites in the triangular primitive unit cell (PUC), as shown in Fig. 1(a). k_n is abbreviated from $\mathbf{k} \cdot \tau_n$ with $\tau_1 = \hat{x}/2$, $\tau_2 = (\hat{x} + \sqrt{3}\hat{y})/4$, and $\tau_3 = \tau_2 - \tau_1$ denoting the three NN vectors. The spectral function of $H_0(\mathbf{k})$ is defined as $A^0(\mathbf{k}, E) = -\frac{1}{\pi}\mathrm{Tr}[\mathrm{Im}\hat{G}^0(\mathbf{k}, iE \to E + i0^+)]$ with $\hat{G}^0(\mathbf{k}, iE) = [iE\hat{I} - \hat{\mathcal{H}}^0_{\mathbf{k}}]^{-1}$. Near the VHF with 1/6 hole doping, the Hamiltonian $\hat{\mathcal{H}}^0_{\mathbf{k}}$ generates the hexagonal FS and the corresponding energy band as shown in Figs. 1(b) and 1(c), respectively, which capture the essential features of the FS and energy band observed in the ARPES experiment and the density functional theory calculations [27].

The second part of the Hamiltonian incorporates the orbital current order,

$$H_{\mathrm{C}} = \sum_{\langle \mathbf{ij}\rangle\alpha} iW_{\mathbf{ij}} c^\dagger_{\mathbf{i}\alpha} c_{\mathbf{j}\alpha}, \tag{4}$$

where $W_{\mathbf{ij}} = -V_c \mathrm{Im}\langle \chi^\dagger_{\mathbf{ij}} \rangle$ denotes the mean-field value of the magnitude of the orbital current order in the CFP with $\chi_{\mathbf{ij}} = c^\dagger_{\mathbf{i}\uparrow} c_{\mathbf{j}\uparrow} + c^\dagger_{\mathbf{i}\downarrow} c_{\mathbf{j}\downarrow}$. The orbital current order could be derived from the Coulomb interaction between electrons on neighboring sites, i.e., $H_V = V_c \sum_{\mathbf{ij}} n_{\mathbf{i}} n_{\mathbf{j}}$ with $n_{\mathbf{i}} = \sum_\alpha c^\dagger_{\mathbf{i}\alpha} c_{\mathbf{i}\alpha}$. A straightforward algebra shows that

$$\begin{aligned} n_{\mathbf{i}} n_{\mathbf{j}} &= 2n_{\mathbf{i}} - \sum_{\alpha\beta} (c^\dagger_{\mathbf{i}\alpha} c_{\mathbf{j}\beta})(c^\dagger_{\mathbf{i}\alpha} c_{\mathbf{j}\beta})^\dagger \\ &= 2n_{\mathbf{i}} - \frac{1}{2}\sum_{\eta=0}^{3} S^\eta_{\mathbf{ij}} \left(S^\eta_{\mathbf{ij}}\right)^\dagger, \end{aligned} \tag{5}$$

where $S^\eta_{\mathbf{ij}} = \sum_{\alpha\beta} c^\dagger_{\mathbf{i}\alpha} \hat{\sigma}^\eta_{\alpha\beta} c_{\mathbf{j}\beta}$. Here, $\hat{\sigma}^0$ is the 2×2 identity matrix and $\hat{\sigma}^{1,2,3}$ are the Pauli matrices. In the Hartree-Fock approximation, we decouple the operator product $S^\eta_{\mathbf{ij}}(S^\eta_{\mathbf{ij}})^\dagger$ with $\langle S^\eta_{\mathbf{ij}}\rangle (S^\eta_{\mathbf{ij}})^\dagger + S^\eta_{\mathbf{ij}} \langle (S^\eta_{\mathbf{ij}})^\dagger \rangle - \langle S^\eta_{\mathbf{ij}}\rangle \langle (S^\eta_{\mathbf{ij}})^\dagger \rangle$. The expectation value $\langle S^\eta_{\mathbf{ij}} \rangle$ defines a four-component vector

$$\left\langle S^\eta_{\mathbf{ij}} \right\rangle = (\langle \chi_{\mathbf{ij}} \rangle, \langle \mathbf{S}_{\mathbf{ij}} \rangle), \tag{6}$$

where the mean-field amplitudes $\langle \chi_{\mathbf{ij}} \rangle$ and $\langle \mathbf{S}_{\mathbf{ij}} \rangle = \langle \sum_{\eta=1}^{3} S^\eta_{\mathbf{ij}} \rangle$ correspond respectively to the currents in the charge and spin channels. For the vanadium-based kagome superconductors, only the charge order is relevant. Thus we need to deal with the case that $\langle \mathbf{S}_{\mathbf{ij}} \rangle = 0$, and this leads to the mean-field decoupling of the NN Coulomb interaction in the charge channel as

$$\begin{aligned} H_{V,MF} = &-\frac{V_c}{2} \sum_{\mathbf{ij}} (\langle \chi^\dagger_{\mathbf{ij}} \rangle \chi_{\mathbf{ij}} + \langle \chi_{\mathbf{ij}} \rangle \chi^\dagger_{\mathbf{ij}} - |\langle \chi_{\mathbf{ij}} \rangle|^2) \\ &+ 2V_c \sum_{\mathbf{i}} n_{\mathbf{i}}. \end{aligned} \tag{7}$$

In this work, we focus on the CDW states with time-reversal symmetry breaking described by the imaginary part of the mean-field value of $\chi_{\mathbf{ij}}$ ($\chi^\dagger_{\mathbf{ij}}$). Using the fact that $\sum_{\mathbf{ij}} \langle \chi^\dagger_{\mathbf{ij}} \rangle \chi_{\mathbf{ij}} = \sum_{\mathbf{ij}} \langle \chi_{\mathbf{ij}} \rangle \chi^\dagger_{\mathbf{ij}}$, we finally arrive at the effective Hamiltonian in Eq. (4). In the procedure for obtaining Eq. (4), we also neglect the constant term $\sum_{\mathbf{ij}} |\langle \chi_{\mathbf{ij}} \rangle|^2$ and absorb the term $2V_c \sum_{\mathbf{i}} n_{\mathbf{i}}$ into the chemical potential.

The third term accounts for the SC pairing. It reads

$$H_{\mathrm{P}} = \sum_{\mathbf{i}} (\Delta c^\dagger_{\mathbf{i}\uparrow} c^\dagger_{\mathbf{i}\downarrow} + \mathrm{H.c.}). \tag{8}$$

Here, we choose the on-site s-wave SC order parameter $\Delta = -V_s \langle c_{\mathbf{i}\downarrow} c_{\mathbf{i}\uparrow} \rangle = V_s \langle c_{\mathbf{i}\uparrow} c_{\mathbf{i}\downarrow} \rangle$. In the calculations, we choose the typical value of the effective pairing interaction $V_s = 1.4$. Varying the pairing interaction will alter the pairing amplitude, but the results presented here will be qualitatively unchanged if the strength of CDW order changes accordingly.

In the coexistence of SC and orbital current orders, the total Hamiltonian $H = H_0 + H_P + H_C$ can be written in the momentum space within one EUC as

$$\begin{aligned} H(\mathbf{k}) = &-t \sum_{\mathbf{k},\langle\tilde{\mathbf{i}}\tilde{\mathbf{j}}\rangle,\sigma} c^\dagger_{\mathbf{k}\tilde{\mathbf{i}}\sigma} c_{\mathbf{k}\tilde{\mathbf{j}}\sigma} e^{-i\mathbf{k}\cdot(\mathbf{r}_{\tilde{i}} - \mathbf{r}_{\tilde{j}})} - \mu \sum_{\mathbf{k},\tilde{\mathbf{i}},\sigma} c^\dagger_{\mathbf{k}\tilde{\mathbf{i}}\sigma} c_{\mathbf{k}\tilde{\mathbf{i}}\sigma} \\ &+ \sum_{\mathbf{k},\langle\tilde{\mathbf{i}}\tilde{\mathbf{j}}\rangle,\sigma} iW_{\tilde{\mathbf{i}}\tilde{\mathbf{j}}} c^\dagger_{\mathbf{k}\tilde{\mathbf{i}}\sigma} c_{\mathbf{k}\tilde{\mathbf{j}}\sigma} e^{-i\mathbf{k}\cdot(\mathbf{r}_{\tilde{i}} - \mathbf{r}_{\tilde{j}})} \\ &+ \sum_{\mathbf{k},\tilde{\mathbf{i}}} (\Delta c^\dagger_{\mathbf{k}\tilde{\mathbf{i}}\uparrow} c^\dagger_{-\mathbf{k}\tilde{\mathbf{i}}\downarrow} + \mathrm{H.c.}), \end{aligned} \tag{9}$$

where $\tilde{\mathbf{i}} \in$ EUC represents the lattice site being within one EUC, and $\langle\tilde{\mathbf{i}}\tilde{\mathbf{j}}\rangle$ denotes the NN bonds with the periodic boundary condition implicitly assumed.

Based on the Bogoliubov transformation, we obtain the following Bogoliubov–de Gennes equations in the EUC,

$$\sum_{\mathbf{k}\tilde{\mathbf{j}}} \begin{pmatrix} H_{\tilde{\mathbf{i}}\tilde{\mathbf{j}},\sigma} & \Delta_{\tilde{\mathbf{i}}\tilde{\mathbf{j}}} \\ \Delta^*_{\tilde{\mathbf{i}}\tilde{\mathbf{j}}} & -H^*_{\tilde{\mathbf{i}}\tilde{\mathbf{j}},\bar{\sigma}} \end{pmatrix} \exp[i\mathbf{k}\cdot(\mathbf{r}_{\tilde{\mathbf{j}}} - \mathbf{r}_{\tilde{\mathbf{i}}})] \begin{pmatrix} u^{\mathbf{k}}_{n,\tilde{\mathbf{j}},\sigma} \\ v^{\mathbf{k}}_{n,\tilde{\mathbf{j}},\bar{\sigma}} \end{pmatrix} = E^{\mathbf{k}}_n \begin{pmatrix} u^{\mathbf{k}}_{n,\tilde{\mathbf{i}},\sigma} \\ v^{\mathbf{k}}_{n,\tilde{\mathbf{i}},\bar{\sigma}} \end{pmatrix}, \tag{10}$$

where $H_{\tilde{\mathbf{i}}\tilde{\mathbf{j}},\sigma} = (-t + iW_{\tilde{\mathbf{i}}\tilde{\mathbf{j}}})\delta_{\tilde{\mathbf{i}}+\tau_{\tilde{\mathbf{j}}},\tilde{\mathbf{j}}} - \mu\delta_{\tilde{\mathbf{i}},\tilde{\mathbf{j}}}$ with $\tau_{\tilde{\mathbf{j}}}$ denoting the four NN vectors and $\Delta_{\tilde{\mathbf{i}}\tilde{\mathbf{j}}} = \Delta\delta_{\tilde{\mathbf{i}},\tilde{\mathbf{j}}}$. $u^{\mathbf{k}}_{n,\tilde{\mathbf{i}},\sigma}$ and $v^{\mathbf{k}}_{n,\tilde{\mathbf{i}},\bar{\sigma}}$ are the Bogoliubov quasiparticle amplitudes on the $\tilde{\mathbf{i}}$th site with momentum $\mathbf{k}$ and eigenvalue $E^{\mathbf{k}}_n$. The amplitudes of the SC pairing and the orbital current order, as well as the electron densities, are obtained through the following self-consistent equations:

$$\begin{aligned}
\Delta &= \frac{V_s}{2}\sum_{\mathbf{k},n} u^{\mathbf{k}}_{n,\tilde{\mathbf{i}},\sigma} v^{\mathbf{k}*}_{n,\tilde{\mathbf{i}},\bar{\sigma}} \tanh\left(\frac{E^{\mathbf{k}}_n}{2k_BT}\right), \\
W_{\tilde{\mathbf{i}}\tilde{\mathbf{j}}} &= \frac{V_c}{2}\mathrm{Im}\Bigg\{\sum_{\mathbf{k},n}\left(u^{\mathbf{k}}_{n,\tilde{\mathbf{i}},\sigma}u^{\mathbf{k}*}_{n,\tilde{\mathbf{j}},\sigma} + v^{\mathbf{k}}_{n,\tilde{\mathbf{i}},\bar{\sigma}}v^{\mathbf{k}*}_{n,\tilde{\mathbf{j}},\bar{\sigma}}\right) \\
&\quad\times \exp[-i\mathbf{k}\cdot(\mathbf{r}_{\tilde{\mathbf{j}}} - \mathbf{r}_{\tilde{\mathbf{i}}})]\tanh\left(\frac{E^{\mathbf{k}}_n}{2k_BT}\right)\Bigg\}, \\
n_{\tilde{\mathbf{i}}} &= \sum_{\mathbf{k},n}\left\{\left|u^{\mathbf{k}}_{n,\tilde{\mathbf{i}},\uparrow}\right|^2 f\left(E^{\mathbf{k}}_n\right) + \left|v^{\mathbf{k}}_{n,\tilde{\mathbf{i}},\downarrow}\right|^2\left[1 - f\left(E^{\mathbf{k}}_n\right)\right]\right\}.
\end{aligned} \tag{11}$$

Due to the fairly good FS nesting, the proximity to the VHF, and the presence of multiple electronic orders, the self-consistent calculations may yield several solutions with local energy minima at the same temperature and doping. In cases where multiple solutions arise from the self-consistent calculations at the same temperature but with different sets of initially random input parameters, we compare their free energy, defined as

$$F = -2k_BT\sum_{\mathbf{k},n,E^{\mathbf{k}}_n>0}\ln\left[2\cosh\left(\frac{E^{\mathbf{k}}_n}{2k_BT}\right)\right] + N\frac{|\Delta|^2}{V_s} + \sum_{\mathbf{k},\langle\tilde{\mathbf{i}}\tilde{\mathbf{j}}\rangle}\frac{|W_{\tilde{\mathbf{i}}\tilde{\mathbf{j}}}|^2}{2V_c}, \tag{12}$$

so as to find the most favorable state in energy.

Then the single-particle Green's functions $G_{\tilde{\mathbf{i}}\tilde{\mathbf{j}}}(\mathbf{k}, i\omega) = -\int_0^\beta d\tau \exp^{i\omega\tau}\langle T_\tau c_{\mathbf{k}\tilde{\mathbf{i}}}(i\tau)c^\dagger_{\mathbf{k}\tilde{\mathbf{j}}}(0)\rangle$ can be expressed as

$$G_{\tilde{\mathbf{i}}\tilde{\mathbf{j}}}(\mathbf{k}, i\omega) = \sum_n\left(\frac{u^{\mathbf{k}}_{n,\tilde{\mathbf{i}},\uparrow}u^{\mathbf{k}*}_{n,\tilde{\mathbf{j}},\uparrow}}{i\omega - E^{\mathbf{k}}_n} + \frac{v^{\mathbf{k}}_{n,\tilde{\mathbf{i}},\downarrow}v^{\mathbf{k}*}_{n,\tilde{\mathbf{j}},\downarrow}}{i\omega + E^{\mathbf{k}}_n}\right). \tag{13}$$

The spectral function $A(\mathbf{k}, E)$ and the DOS $\rho(E)$ can be derived from the analytic continuation of the Green's function as

$$A(\mathbf{k}, E) = -\frac{1}{N_P\pi}\sum_{\tilde{\mathbf{i}}}\mathrm{Im}G_{\tilde{\mathbf{i}}\tilde{\mathbf{i}}}(\mathbf{k}, iE \to E + i0^+), \tag{14}$$

and

$$\rho(E) = \frac{1}{N_{\mathbf{k}}}\sum_{\mathbf{k}}A(\mathbf{k}, E), \tag{15}$$

where N_P and $N_{\mathbf{k}}$ are the number of PUCs in the EUC and the number of $\mathbf{k}$ points in the Brillouin zone, respectively.

III. RESULTS AND DISCUSSION

A. Phase diagram

In the following analysis, the chemical potential μ is adjusted to achieve the desired filling. Right at the VHF, the FS possesses a hexagonal shape, with the saddle points M_A, M_B and M_C located exactly on the FS. This unique FS possesses a perfect nesting property and facilitates the interscatterings between three VHSs connected by the nesting vectors $\mathbf{Q}_a = (-\pi, \sqrt{3}\pi)$, $\mathbf{Q}_b = (-\pi, -\sqrt{3}\pi)$, and $\mathbf{Q}_c = (2\pi, 0)$, which has been considered as the primary factors promoting the so-called "triple-Q" 2×2 CDW in AV_3Sb_5 [27,34,37,38,40,64,74]. Away from the VHF, the FS becomes more rounded, and the nesting is weakened, particularly around the saddle points [M_A, M_B and M_C in Fig. 1(b)]. We focus on the situation where the hole doping is deceased from 1/6, such that the saddle points move slightly below the Fermi level as displayed in Figs. 1(c) and 1(d), being consistent with the density functional theory calculations [37,96–98].

As a function of doping and temperature, we find a rich phase diagram of the model at and near the VHF, which is summarized in Fig. 2(a) for the typical values of $V_s = 1.4$ and $V_c = 1.2$. Right at the VHF for 1/6 doping, where the DOS at the Fermi level is maximally enhanced and the nesting features of the FS are strongest, the system prefers the TCFP [Fig. 2(b)] before entering the SC state. Once the system deviates from the VHF, the NCFP order [Fig. 2(c)] develops in between the TCFP and the low-temperature SC state. In this case, when decreasing the temperature, the system starts from the high-temperature normal state and passes through the NCFP state, and finally transits into the SC state. When the filling further departs from the van Hove point, the region of the NCFP expands gradually towards higher temperatures with the concomitant shrinking of the TCFP region, and eventually the TCFP is completely displaced by the NCFP state. Interestingly, the SC state always coexists with the NCFP state in the low temperature region of the phase diagram, with its free energy being significantly lower than those of the pure states. Although the reasonable variations of V_s and V_c may affect the phase boundaries, the essential feature of the phase diagram, namely, the consecutive evolvement of different ordered states with temperature, remains qualitatively unchanged.

It is remarkable that the successive temperature evolutions from the TCFP phase to the NCFP state, occurring at a doping level slightly deviating from the van Hove point in a self-consistent manner, exhibits the same trend as the experimental

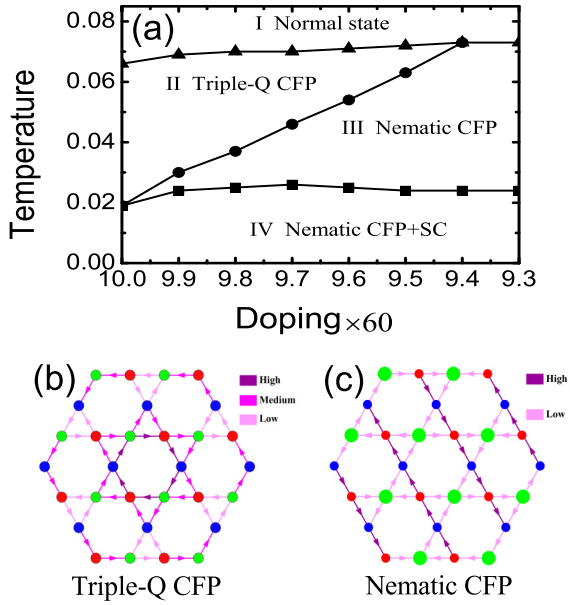

FIG. 2. (a) Phase diagram as a function of doping and temperature. The orbital current configurations for (b) the "triple-Q" CFP and (c) the nematic CFP. The arrows in panel (b) with their respective colors indicated by the labels of "High," "Medium," and "Low" signal the magnitudes of the bond current orders. The arrows in panel (c) with their respective colors indicated by the labels of "High" and "Low" signal the magnitudes of the bond current orders. In panel (c), the large (green dots) and small (red and blue dots) sizes of lattice site also signal respectively the "High" and "Low" values of the on-site SC pairing amplitude in the coexisting phase (see text and Table II for reference).

observations [57,62,90,91]. Particularly, the ground state characterized by the coexistence of the NCFP and SC orders may be related to the C_2 symmetry and the time-reversal symmetry breaking observed in the SC state [37,45,62].

Since the effect of doping on the phase diagram is closely related to the VHF, we focus on the physics associated with the three van Hove points, in addition to a nesting properties of the FS. At each van Hove point, the electronic states come exclusively from one of the three distinct sublattices [10]. As a result, the scattering between low-energy electronic states connected by each nesting wave vector occurs solely between two sublattices. This unique property creates the necessary conditions for the transition from the TCFP to the NCFP through doping. At VHF, the electronic states at the three van Hove points are mutually coupled by the CDW orders with three wave vectors $\mathbf{Q}_a$, $\mathbf{Q}_b$, and $\mathbf{Q}_c$ in the TCFP in an end-to-end manner [Fig. 1(b)]. This is to say, the CDW orders with three wave vectors are mutually coupled in pairs with the strongest coupling strength at the van Hove points. Thus, as depicted in the phase diagram [Fig. 2(a)], a stable charge order pattern that simultaneously satisfies the three wave vectors can be found at the VHF.

However, when the system deviates from the VHF by reducing the hole doping, the chemical potential μ is elevated, and accordingly the saddle points move below the Fermi level, as demonstrated in Figs. 1(c) and 1(d). The deviation of the FS from the saddle points weakens the mutual couplings between pairs of the three wave vectors and, correspondingly,

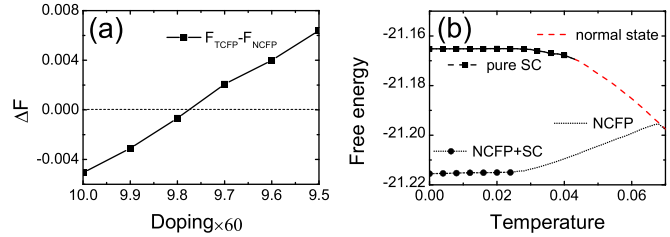

FIG. 3. (a) Doping dependence of the free-energy difference per site between the "triple-Q" CFP and nematic CFP. In obtaining the results in panel (a), the CDW states are each intentionally kept in their respective forms during the calculations. (b) The evolutions of the free energy per site from the normal state (dashed line) to pure SC state (dashed line with square symbol) and from the nematic CFP (dotted line) to the coexisting phase with nematic CFP and SC state (dotted line with round symbol) at doping level 9.8/60.

the TCFP. In this situation, there is a significant decrease in the energy difference between the TCFP, which satisfies three ordered wave vectors, and the NCFP, which has only one ordered wave vector. Moreover, the NCFP will deform the FS, suppressing the other two NCFP with different ordered wave vectors while further enhancing itself [refer to Figs. 2(c) and 4(b) and Table I]. Consequently, within a certain doping range, the NCFP becomes more stable than the TCFP. For better clarity, we present the evolutions of the free-energy difference between the TCFP and the NCFP with doping at a specific temperature $T = 0.04$ in Fig. 3(a). It shows that the TCFP has a lower free energy than that of the NCFP, when the doping level has not much deviations from the VHF. Nevertheless, as the system deviates appreciably from the VHF, the NCFP acquires the lower free energy. As a result, a spontaneous rotational-symmetry-breaking transition occurs from the TCFP to the NCFP at the doping level defined by the zero point of the free-energy difference. Across the transition, the self-consistent results of the CDW order parameters change discontinuously, and thus it belongs to the first-order phase transition for the present model calculations.

The temperature effects on the CDW states are also closely related to the van Hove physics. Although the van Hove points shift below the Fermi level for doping levels deviating from the VHF, the thermal broadening effect becomes prominent at relatively high temperatures, thereby increasing the effectiveness of the van Hove points. This enhances the mutual coupling among three CDW orders associated with different wave vectors $\mathbf{Q}_a$, $\mathbf{Q}_b$, and $\mathbf{Q}_c$. As a result, for doping levels that deviate from the VHF, the TCFP is stabilized by the thermal broadening effect at relatively high temperatures, while the NCFP becomes more favorable due to the reduction of thermal broadening effect at low temperatures.

TABLE I. Magnitude of the bond current order $|W_{ij}|$ in the self-consistent calculations at doping level 9.8/60 with $T = 0.05$ for the "triple-Q" CFP and $T = 0.03$ for the nematic CFP.

	High	Medium	Low
"Triple-Q" CFP	0.043805	0.035128	0.026666
Nematic CFP	0.071768		0.00841

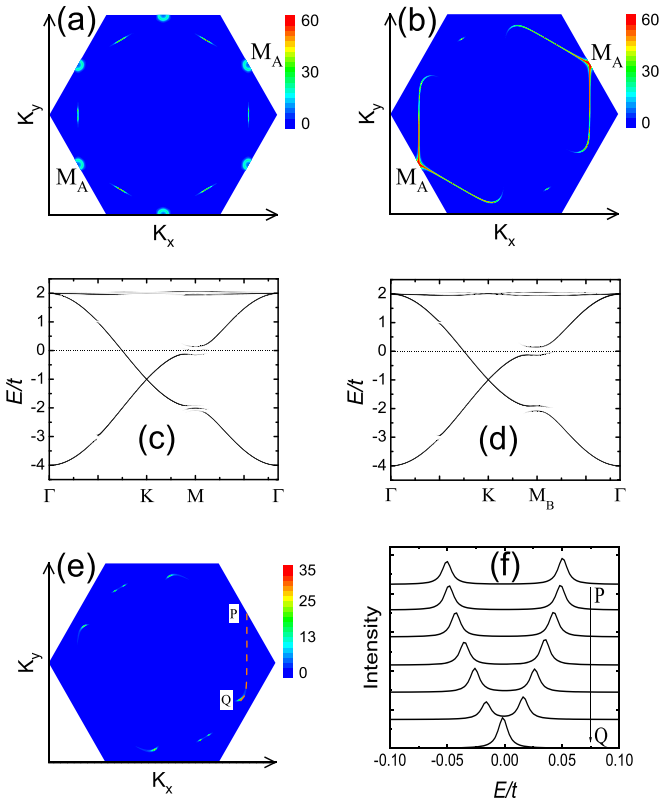

FIG. 4. Zero-energy spectral weight distribution $A(\mathbf{k}, E)$ unfolded in the primitive Brillouin zone for hole doping 9.8/60 at (a) $T = 0.05$, and (b) $T = 0.03$. The former situates in the "triple-Q" CFP region, while the latter lies in the region of the nematic CFP state. The unfolded dispersions along high-symmetry cuts in the primitive Brillouin zone are shown correspondingly in panel (c) for the "triple-Q" CFP state, and in panel (d) for the nematic CFP state, respectively. (e) Zero-energy spectral weight distribution $A(\mathbf{k}, E)$ unfolded in the primitive Brillouin zone at hole doping 9.8/60 with $T = 1 \times 10^{-5}$ for the coexisting phase of the nematic CFP and SC orders. (f) Energy distribution curves of the spectra at a series of momentum point along the momentum cut from P to Q shown by the dashed orange line in panel (e). The curves in panel (f) are vertically shifted for clarity.

Previously, the transition to the CDW with C_2 symmetry was proposed to arise from interlayer interactions between adjacent kagome planes with already existing C_6-symmetry charge orders in each single layer [96,99]. As a secondary outcome of the C_6-symmetry charge orders in this interlayer coupling scenario, the nematicity typically occurs at a lower temperature T_{nem}, well below T_{CDW}. However, as shown in Fig. 2(a), our theory shows a regime of less than 9.4/60 hole doping where the NCFP directly straddles the normal and SC states, despite in the high doping level regime of the phase diagram the appearance of nematic CDW at low temperatures is well below T_{CDW}. Interestingly, a recent experiment has indeed observed an immediate development of nematicity and possible time-reversal symmetry breaking in the CDW state of CsV_3Sb_5 [92], providing further support of our theory.

As the temperature continues to decrease, several ingredients promote the development of the coexisting phase of the NCFP and SC state. First of all, as depicted in Figs. 3(b)

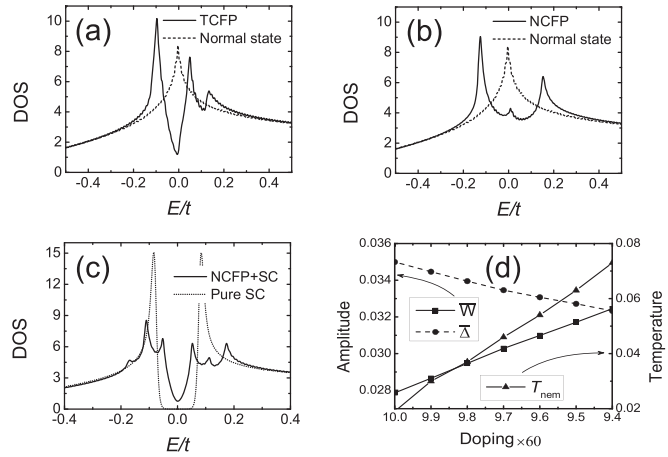

FIG. 5. Energy dependence of the DOSs for (a) the "triple-Q" CFP, (b) the nematic CFP, and (c) the coexisting phase of the nematic CFP and SC orders, respectively. (d) The doping dependence of the averaged SC pairing amplitude $\bar{\Delta}$, the averaged magnitude of the bond current orders $\bar{W}$, and the transition temperature of the nematic CFP T_{nem}.

and 6(a), the NCFP exhibits a lower energy compared with the normal and TCFP states before the SC transition, making it energetically favorable as the parent state for the formation of the SC order. Second, the well-preserved portions of the FS, especially those portions near the saddle points [the M_A points in Fig. 4(b)], within the NCFP provide sufficient electronic states for the formation of the SC pairing. Third, apart from the gaped portions of the FS, the one-wave-vector scattering with the rotational symmetry breaking in the NCFP state induces a slight deformation of the FS [refer to Figs. 4(b) and 6(b)], which brings the remaining FS closer to the van Hove points compared with the normal state. As a result, the coexisting phase of NCFP and SC orders possesses the significantly lower free energy than that for the pure SC state [see Fig. 3(b)].

B. Characteristics of electronic states

Next, we investigate in detail on the electronic structures in different regime of the phase diagram, namely, the TCFP state, the NCFP state, and the coexisting state of the NCFP and SC orders. To demonstrate our results, we focus on the typical cases with a doping level of 9.8/60 at temperatures $T = 0.05$, $T = 0.03$, and $T = 1 \times 10^{-5}$, corresponding to the TCFP state, the NCFP state and the coexisting phase of the NCFP and SC orders, respectively.

For the TCFP, the bond current orders obtained from self-consistent calculations can be classified into three levels of magnitude: "High," "Medium," and "Low," as displayed in Fig. 2(b) and listed in Table I. These orders give rise to a special pattern known as the "Star of David" state. Figure 4(a) presents the distribution of spectral weight $A(\mathbf{k}, E)$ at $E = 0$, which is unfolded in the primitive Brillouin zone. Consistent with the previous nonself-consistent results [95], the zero-energy spectral weight distribution clearly reveals partially gapped Fermi segments and preserves the C_6 symmetry. Correspondingly, the DOS shown in Fig. 5(a) exhibits

a "pseudogap-like" feature, with nonzero minima occurring at $E = 0$. In contrast, the DOS for the normal state, represented by the black dashed curve in the same figure, displays the typical van Hove peak near $E = 0$.

On the other hand, as the temperature decreases into the NCFP regime, such as $T = 0.03$, the magnitude distribution of the three inequivalent bond current orders transforms into that of two inequivalent orders. The "Low" intensity is associated with two inequivalent bonds, which are approximately one order of magnitude smaller than the other one labeled as "High" intensity. In this case, only the strong current order between sublattices B and C corresponds to the charge order scattering between M_B and M_C points with a momentum transfer $\mathbf{Q}_a$. As a result, the depletion of the zero-energy spectral weight only occurs in regions connected by one of the three wave vectors, such as $\mathbf{Q}_a$ in Fig. 4(b), manifesting the characteristics of the C_2 symmetry. Meanwhile, the depletion of spectral weight can also diminish the particle-hole scatterings linked to $\mathbf{Q}_b$ and $\mathbf{Q}_c$, correspondingly suppressing the bond orders associated with these two wave vectors and enhancing the bond order associated with $\mathbf{Q}_a$. As the system deviates from the VHF weakening the mutual couplings between pairs of the three wave vectors, such an antagonistic relationship among the three bond orders tips the balance toward an NCFP state. The DOS for the NCFP depicted by the black solid curve in Fig. 5(b) still exhibits two peaks resembling gap edges, but a significant DOS shows up within the peak edges, accompanied by a residue van Hove peak near the zero bias, resulting from the large portion of the unspoilt Fermi segments and the preserved van Hove points M_A.

Let us further analyze the characteristics of the band structures in the two CDW states. In the TCFP, the bands along different high-symmetry cuts $\Gamma \to K$ (or K') $\to$ M_A (or M_B or M_c) $\to \Gamma$ remain the same due to the preservation of the C_6 symmetry, while in the NCFP, a gap opens near the M_B and M_C points but not near the M_A point, as shown in Figs. 4(d), 7(a), and 7(b). In addition, near the saddle point, the band is triply split in the TCFP, while it is only doubly split near the M_B and M_C points in the NCFP, as illustrated in Figs. 4(c), 4(d), and 7(a). This behavior can be understood through the "patch model," which provides an approximate description of the low-energy scatterings between the saddle points [100–102]. In the TCFP state, the patch model involving the "triple-Q" scatterings reads,

$$H_{\mathrm{TCFP}}(M) = \begin{pmatrix} \varepsilon_{M_A} & i\lambda_{AB} & i\lambda_{AC} \\ -i\lambda_{AB} & \varepsilon_{M_B} & i\lambda_{BC} \\ -i\lambda_{AC} & -i\lambda_{BC} & \varepsilon_{M_C} \end{pmatrix}. \tag{16}$$

Nevertheless, the charge order scattering in the NCFP involves only one wave vector, such as $\mathbf{Q}_a$ that corresponds to the bond current configuration in Fig. 2(c). As a result, the patch model in the NCFP state is reduced to

$$H_{NCFP}(M) = \begin{pmatrix} \varepsilon_{M_B} & i\lambda_{BC} \\ -i\lambda_{BC} & \varepsilon_{M_C} \end{pmatrix}. \tag{17}$$

Here, ε_{M_A} (ε_{M_B}, ε_{M_C}) stands for the energy at the saddle point M_A (M_B, M_C) that originates from the sublattice A (B, C), and λ_{AB} (λ_{AC}, λ_{BC}) represents the scattering strength of the bond current order between M_A and M_B (M_A and M_C, M_B and M_C). Near the VHF, where $\varepsilon_{M_A} = \varepsilon_{M_B} = \varepsilon_{M_C} \approx 0$, one can immediately find that the Hamiltonian $H_{\mathrm{TCFP}}(M)$ has three eigenvalues $E_0(M) = 0$ and $E_\pm(M) = \pm(\lambda_{AB}^2 + \lambda_{AC}^2 + \lambda_{BC}^2)^{1/2}$. The Hamiltonian $H_{NCFP}(M)$, on the other hand, has two eigenvalues $E_\pm(M) = \pm|\lambda_{BC}|$. It is worth pointing out that the unique change of the electronic structures from the TCFP to the NCFP can serve as an indirect evidence to identify the electronic nematicity in AV_3Sb_5.

TABLE II. Magnitudes of the bond current order $|W_{ij}|$ and the SC pairing $|\Delta|$ in the self-consistent calculations at doping level 9.8/60 with $T = 1 \times 10^{-5}$ for the coexisting phase of the nematic CFP and SC orders.

	High	Low
Nematic CFP	0.072113	0.008144
SC	0.050711	0.025567

Then, we turn to the coexisting phase of the NCFP and SC orders. On the one hand, as indicated in Table II, the strength of the bond current orders changes little upon entering the coexisting phase. On the other hand, as displayed in Fig. 2(c), the distribution of SC pairing amplitudes depends not only on the strength but also on the direction of the surrounding bond current orders. Specifically, the "High" value of the SC pairing amplitude appears at the sublattice site [the sublattice A in Fig. 2(c)] where the surrounding bond current orders are weak and the bonds connected to the same sublattice sites carry either the same inflow current directions or the same outflow current directions. On the contrary, the "Low" value of the SC pairing amplitude appears on the sublattice sites where a pair of bonds connected to the same sublattice sites have respective inflow and outflow current directions. The uneven distribution of the SC pairing amplitude can be understood from the low-energy spectral distribution shown in Fig. 4(b). In the coexisting phase of the NCFP and SC orders, since the depletion of the low-energy spectral weight only occurs at portions between M_B and M_C, the remaining spectral weights, including the perfect van Hove points M_A caused by the deformation of the FS, mainly come from the sublattice A. Consequently, the SC pairing amplitude on sublattice A is significantly larger than those on the sublattices B and C.

Remarkably, the nonuniform distributions of the SC pairing amplitude and the scattering of the CDW order could lead to variations and even nodal structure of the SC gap along the FS as well, even though a conventional on-site SC pairing is considered here. In the coexisting phase of the NCFP and SC orders, whereas the most part of the remnant FSs shown in Fig. 4(b) is gaped by the SC order, significant spectral weight still remains at point Q and its symmetric points, as demonstrated in Fig. 4(e), depicting a nodal SC state. The nodal structure and variations of the SC gap are more visible in the energy distribution curves of the spectra for a series of momentum point on the FS from P to Q, denoted by the dashed orange line in Fig. 4(e). As depicted in Fig. 4(f), the largest SC gap appears at the momentum point P, i.e., the M_A point in Fig. 4(b), which is located furthest from the NCFP scatterings. The SC gap exhibits a gradual decrease as the momentum cut moves away from the P point and finally reaches a zero-gap structure at the nodal point Q, which

is the closest point on the remnant FS to the NCFP gap. As a result, a V-shaped DOS can be observed in Fig. 5(c), accompanied by multiple sets of coherent peaks and residual zero-energy DOS, constituting a characteristic of a nodal multigap SC pairing state as having been observed in the STM experiments [38–40]. For comparison, the dotted curve in the same figure portrays a typical U-shaped full gap structure for the DOS in the state with pure on-site *s*-wave SC pairing, which is obtained by excluding the CDW term from the Hamiltonian.

Considering the nature of the mean-field approximation, it should be noted that the transition temperature between different phases in the calculated results is just qualitative rather than quantitative. Nevertheless, the anticorrelation trend between the SC pairing amplitude and the transition temperature of the nematic phase at different doping levels can be clearly observed in Fig. 5(d), as supported by the STM experiments [91].

It should be noted that, in actual materials, factors such as electron-phonon coupling and anharmonic effects are expected to play some roles in the phase transition [103–106]. Nevertheless, the nearly perfect FS nesting and the presence of VHSs in the vicinity of the Fermi energy significantly enhance the electronic correlations in this family of materials, and thus make the model-specific results of the CDW formation and the interpretation of the phase transition based on the mechanism of FS nesting and the electronic interactions experimentally relevant.

One other thing to note is that the present results are based on a single orbital kagome tight-binding model with the Fermi level approaching the upper VHSs, the so-called *p*-type singularities [66,67,75]. Recent ARPES experiments revealed two types of singularities coexisting near the Fermi level, i.e., the *p*-type and *m*-type singularities [49], which originate respectively from the pure and mixed sublattice characters. This distinction leads to distinct sublattice interference effects for the two types of van Hove singularities, thereby impacting the interplay between CDW and superconductivity. Notably, the *m*-type singularities exhibit a less pronounced effect on reducing the on-site interaction compared with the *p*-type ones. How and to what extent does the *m*-type singularity influence on the delicate interplay between the SC and CDW states in a two-orbital model, containing simultaneously the *p*- and *m*-type singularities near the Fermi level, constitutes another fascinating questions being worthy of further research.

IV. CONCLUSION

In conclusion, we have investigated the origin of the chiral CDW and its interplay with superconductivity in a fully self-consistent theory considering the orbital current order and the on-site SC pairing, which determines both the CDW and the SC orders self-consistently. It was revealed that the self-consistent theory captures the salient feature for the successive temperature evolutions of the ordered electronic states from the high-temperature 2×2 TCFP to the NCFP, and to the low-temperature *s*-wave SC state in a coexisting manner with the NCFP order. The rotational-symmetry-breaking transition of the CDW could be understood from a scenario in which the competition between the deviation from the VHF and the thermal broadening of the FS determines which state it is in. The intertwining of the *s*-wave SC pairing with the NCFP order produced a nodal gap feature manifesting as the V-shaped DOS along with the residual DOS near the Fermi energy. The self-consistent theory not only produces the successive temperature evolutions of the electronically ordered states observed in experiment, but might also offer a heuristic explanation of the twofold rotational symmetry of electron state detected in both the CDW and the SC states. Moreover, the intertwining of the SC pairing with the NCFP order, which was found to be a ground state in the self-consistent theory at the low-temperature regime, might also be a promising alternative for mediating the divergent or seemingly contradictory experimental outcomes regarding the SC properties. Overall, our study sheds light on the intricate relationship between the chiral CDW and superconductivity, providing valuable insights into the underlying mechanisms and experimental observations.

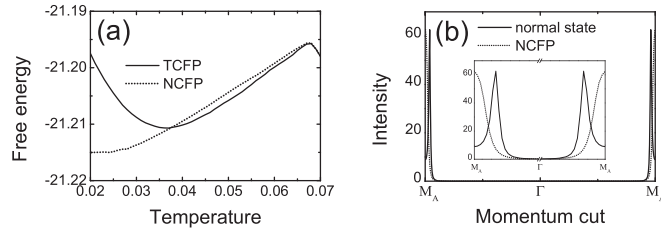

FIG. 6. (a) Temperature evolution of the free energy per site for the doping level 9.8/60 in the "triple-Q" CFP (solid line) and in the nematic CFP (dotted line). In obtaining the results in panel (a), the CDW states are intentionally kept in their respective forms during the calculations. (b) The momentum cut of the spectral weight along the $M_A \rightarrow \Gamma \rightarrow M_A$ direction at a doping level deviating from the VHF for the normal state (solid curve) and for the nematic CFP (dotted curve). The peaks of the spectral weight intensity denote the position of the Fermi surface [refer to Fig. 4(b) in the main text]. The same figure as panel (b) is replotted in the inset by breaking the x axis in order to have a better view of the Fermi-surface shift.

ACKNOWLEDGMENTS

This work was supported by National Key Projects for Research and Development of China (Grant No. 2021YFA1400400) and the National Natural Science Foundation of China (Grants No. 12074175, No. 12374137, and No. 92165205).

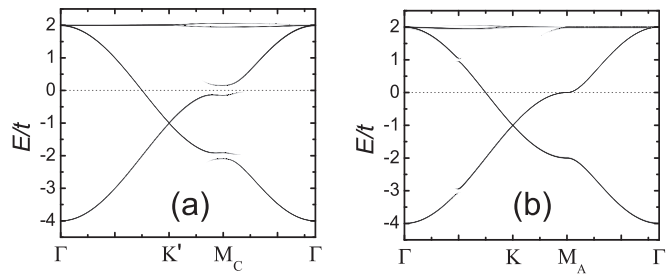

FIG. 7. The unfolded dispersions along high-symmetry cuts (a) Γ-K'-M_C-Γ and (b) Γ-K-M_A-Γ.

APPENDIX: TEMPERATURE EVOLUTION OF FREE ENERGY, DETAILS OF SPECTRUM, AND BAND STRUCTURE ALONG HIGH-SYMMETRY CUTS

In Fig. 6(a), we show the temperature evolution of the free energy in the TCFP and in the NCFP. In Fig. 6(b), we display the momentum cut of the spectral weight along the $M_A \rightarrow \Gamma \rightarrow M_A$ direction [see Fig. 4(b) in the main text] at a doping level deviating from the VHF for the normal state and for the NCFP.

In Fig. 7, we present the unfolded dispersions of the spectral weight along different high-symmetry cuts for the NCFP. Owing to the C_2 symmetry of the NCFP, the energy bands exhibit different features along different high-symmetry cuts. Specifically, an energy gap opens near the M_B and M_C points but not near the M_A point, as presented respectively in Figs. 7(a) and 7(b).

[1] Y. Ran, M. Hermele, P. A. Lee, and X.-G. Wen, Phys. Rev. Lett. **98**, 117205 (2007).
[2] H. C. Jiang, Z. Y. Weng, and D. N. Sheng, Phys. Rev. Lett. **101**, 117203 (2008).
[3] S. Yan, D. A. Huse, and S. R. White, Science **332**, 1173 (2011).
[4] S. Depenbrock, I. P. McCulloch, and U. Schollwöck, Phys. Rev. Lett. **109**, 067201 (2012).
[5] T.-H. Han, J. S. Helton, S. Chu, D. G. Nocera, J. A. Rodriguez-Rivera, C. Broholm, and Y. S. Lee, Nature (London) **492**, 406 (2012).
[6] Y.-C. He, D. N. Sheng, and Y. Chen, Phys. Rev. Lett. **112**, 137202 (2014).
[7] H. J. Liao, Z. Y. Xie, J. Chen, Z. Y. Liu, H. D. Xie, R. Z. Huang, B. Normand, and T. Xiang, Phys. Rev. Lett. **118**, 137202 (2017).
[8] Z. Feng, Z. Li, X. Meng, W. Yi, Y. Wei, J. Zhang, Y.-C. Wang, W. Jiang, Z. Liu, S. Li, F. Liu, J. Luo, S. Li, G.-q. Zheng, Z. Y. Meng, J.-W. Mei, and Y. Shi, Chin. Phys. Lett. **34**, 077502 (2017).
[9] P. Khuntia, M. Velazquez, Q. Barthélemy, F. Bert, E. Kermarrec, A. Legros, B. Bernu, L. Messio, A. Zorko, and P. Mendels, Nat. Phys. **16**, 469 (2020).
[10] S.-L. Yu and J.-X. Li, Phys. Rev. B **85**, 144402 (2012).
[11] M. L. Kiesel and R. Thomale, Phys. Rev. B **86**, 121105(R) (2012).
[12] M. L. Kiesel, C. Platt, and R. Thomale, Phys. Rev. Lett. **110**, 126405 (2013).
[13] W.-S. Wang, Z.-Z. Li, Y.-Y. Xiang, and Q.-H. Wang, Phys. Rev. B **87**, 115135 (2013).
[14] W.-H. Ko, P. A. Lee, and X.-G. Wen, Phys. Rev. B **79**, 214502 (2009).
[15] J. Kang, S.-L. Yu, Z.-J. Yao, and J.-X. Li, J. Phys.: Condens. Matter **23**, 175702 (2011).
[16] H.-M. Guo and M. Franz, Phys. Rev. B **80**, 113102 (2009).
[17] S.-L. Yu, J.-X. Li, and L. Sheng, Phys. Rev. B **80**, 193304 (2009).
[18] J. Wen, A. Rüegg, C.-C. J. Wang, and G. A. Fiete, Phys. Rev. B **82**, 075125 (2010).
[19] E. Tang, J.-W. Mei, and X.-G. Wen, Phys. Rev. Lett. **106**, 236802 (2011).
[20] G. Xu, B. Lian, and S.-C. Zhang, Phys. Rev. Lett. **115**, 186802 (2015).
[21] L. Ye, M. Kang, J. Liu, F. v. Cube, C. R. Wicker, T. Suzuki, C. Jozwiak, A. Bostwick, E. Rotenberg, D. C. Bell, L. Fu, R. Comin, and J. G. Checkelsky, Nature (London) **555**, 638 (2018).
[22] D. F. Liu, A. J. Liang, E. K. Liu, Q. N. Xu, Y. W. Li, C. Chen, D. Pei, W. J. Shi, S. K. Mo, P. Dudin, T. Kim, C. Cacho, G. Li, Y. Sun, L. X. Yang, Z. K. Liu, S. S. P. Parkin, C. Felser, and Y. L. Chen, Science **365**, 1282 (2019).
[23] J.-X. Yin, W. Ma, T. A. Cochran, X. Xu, S. S. Zhang, H.-J. Tien, N. Shumiya, G. Cheng, K. Jiang, B. Lian, Z. Song, G. Chang, I. Belopolski, D. Multer, M. Litskevich, Z.-J. Cheng, X. P. Yang, B. Swidler, H. Zhou, H. Lin, T. Neupert, Z. Wang, N. Yao, T.-R. Chang, S. Jia, and M. Z. Hasan, Nature (London) **583**, 533 (2020).
[24] A. Rüegg and G. A. Fiete, Phys. Rev. B **83**, 165118 (2011).
[25] S. V. Isakov, S. Wessel, R. G. Melko, K. Sengupta, and Y. B. Kim, Phys. Rev. Lett. **97**, 147202 (2006).
[26] Y.-M. Wu, R. Thomale, and S. Raghu, Phys. Rev. B **108**, L081117 (2023).
[27] B. R. Ortiz, S. M. L. Teicher, Y. Hu, J. L. Zuo, P. M. Sarte, E. C. Schueller, A. M. Milinda Abeykoon, M. J. Krogstad, S. Rosenkranz, R. Osborn, R. Seshadri, L. Balents, J. He, and S. D. Wilson, Phys. Rev. Lett. **125**, 247002 (2020).
[28] S.-Y. Yang, Y. Wang, B. R. Ortiz, D. Liu, J. Gayles, E. Derunova, R. Gonzalez-Hernandez, L. Šmejkal, Y. Chen, S. S. P. Parkin, S. D. Wilson, E. S. Toberer, T. McQueen, and M. N. Ali, Sci. Adv. **6**, eabb6003 (2020).
[29] B. R. Ortiz, P. M. Sarte, E. M. Kenney, M. J. Graf, S. M. L. Teicher, R. Seshadri, and S. D. Wilson, Phys. Rev. Mater. **5**, 034801 (2021).
[30] Q. Yin, Z. Tu, C. Gong, Y. Fu, S. Yan, and H. Lei, Chin. Phys. Lett. **38**, 037403 (2021).
[31] K. Y. Chen, N. N. Wang, Q. W. Yin, Y. H. Gu, K. Jiang, Z. J. Tu, C. S. Gong, Y. Uwatoko, J. P. Sun, H. C. Lei, J. P. Hu, and J.-G. Cheng, Phys. Rev. Lett. **126**, 247001 (2021).
[32] Y. Wang, S. Yang, P. K. Sivakumar, B. R. Ortiz, S. M. L. Teicher, H. Wu, A. K. Srivastava, C. Garg, D. Liu, S. S. P. Parkin, E. S. Toberer, T. McQueen, S. D. Wilson, and M. N. Ali, Sci. Adv. **9**, eadg7269 (2023).
[33] Z. Zhang, Z. Chen, Y. Zhou, Y. Yuan, S. Wang, J. Wang, H. Yang, C. An, L. Zhang, X. Zhu, Y. Zhou, X. Chen, J. Zhou, and Z. Yang, Phys. Rev. B **103**, 224513 (2021).
[34] Y.-X. Jiang, J.-X. Yin, M. M. Denner, N. Shumiya, B. R. Ortiz, G. Xu, Z. Guguchia, J. He, M. S. Hossain, X. Liu, J. Ruff, L. Kautzsch, S. S. Zhang, G. Chang, I. Belopolski, Q. Zhang, T. A. Cochran, D. Multer, M. Litskevich, Z.-J. Cheng, X. P. Yang, Z. Wang, R. Thomale, T. Neupert, S. D. Wilson, and M. Z. Hasan, Nat. Mater. **20**, 1353 (2021).
[35] F. H. Yu, T. Wu, Z. Y. Wang, B. Lei, W. Z. Zhuo, J. J. Ying, and X. H. Chen, Phys. Rev. B **104**, L041103 (2021).

[36] X. Chen, X. Zhan, X. Wang, J. Deng, X.-B. Liu, X. Chen, J.-G. Guo, and X. Chen, Chin. Phys. Lett. **38**, 057402 (2021).

[37] H. Zhao, H. Li, B. R. Ortiz, S. M. L. Teicher, T. Park, M. Ye, Z. Wang, L. Balents, S. D. Wilson, and I. Zeljkovic, Nature (London) **599**, 216 (2021).

[38] H. Chen, H. Yang, B. Hu, Z. Zhao, J. Yuan, Y. Xing, G. Qian, Z. Huang, G. Li, Y. Ye, S. Ma, S. Ni, H. Zhang, Q. Yin, C. Gong, Z. Tu, H. Lei, H. Tan, S. Zhou, C. Shen, X. Dong, B. Yan, Z. Wang, and H.-J. Gao, Nature (London) **599**, 222 (2021).

[39] H.-S. Xu, Y.-J. Yan, R. Yin, W. Xia, S. Fang, Z. Chen, Y. Li, W. Yang, Y. Guo, and D.-L. Feng, Phys. Rev. Lett. **127**, 187004 (2021).

[40] Z. Liang, X. Hou, F. Zhang, W. Ma, P. Wu, Z. Zhang, F. Yu, J.-J. Ying, K. Jiang, L. Shan, Z. Wang, and X.-H. Chen, Phys. Rev. X **11**, 031026 (2021).

[41] C. Mu, Q. Yin, Z. Tu, C. Gong, H. Lei, Z. Li, and J. Luo, Chin. Phys. Lett. **38**, 077402 (2021).

[42] C. C. Zhao, L. S. Wang, W. Xia, Q. W. Yin, J. M. Ni, Y. Y. Huang, C. P. Tu, Z. C. Tao, Z. J. Tu, C. S. Gong, H. C. Lei, Y. F. Guo, X. F. Yang, and S. Y. Li, arXiv:2102.08356.

[43] S. Ni, S. Ma, Y. Zhang, J. Yuan, H. Yang, Z. Lu, N. Wang, J. Sun, Z. Zhao, D. Li, S. Liu, H. Zhang, H. Chen, K. Jin, J. Cheng, L. Yu, F. Zhou, X. Dong, J. Hu, H.-J. Gao, and Z. Zhao, Chin. Phys. Lett. **38**, 057403 (2021).

[44] W. Duan, Z. Nie, S. Luo, F. Yu, B. R. Ortiz, L. Yin, H. Su, F. Du, A. Wang, Y. Chen, X. Lu, J. Ying, S. D. Wilson, X. Chen, Y. Song, and H. Yuan, Sci. China: Phys., Mech. Astron. **64**, 107462 (2021).

[45] Y. Xiang, Q. Li, Y. Li, W. Xie, H. Yang, Z. Wang, Y. Yao, and H.-H. Wen, Nat. Commun. **12**, 6727 (2021).

[46] B. R. Ortiz, S. M. L. Teicher, L. Kautzsch, P. M. Sarte, N. Ratcliff, J. Harter, J. P. C. Ruff, R. Seshadri, and S. D. Wilson, Phys. Rev. X **11**, 041030 (2021).

[47] X. Zhou, Y. Li, X. Fan, J. Hao, Y. Dai, Z. Wang, Y. Yao, and H.-H. Wen, Phys. Rev. B **104**, L041101 (2021).

[48] Z. Liu, N. Zhao, Q. Yin, C. Gong, Z. Tu, M. Li, W. Song, Z. Liu, D. Shen, Y. Huang, K. Liu, H. Lei, and S. Wang, Phys. Rev. X **11**, 041010 (2021).

[49] M. Kang, S. Fang, J.-K. Kim, B. R. Ortiz, S. H. Ryu, J. Kim, J. Yoo, G. Sangiovanni, D. D. Sante, B.-G. Park, C. Jozwiak, A. Bostwick, E. Rotenberg, E. Kaxiras, S. D. Wilson, J.-H. Park, and R. Comin, Nat. Phys. **18**, 301 (2022).

[50] Y. Fu, N. Zhao, Z. Chen, Q. Yin, Z. Tu, C. Gong, C. Xi, X. Zhu, Y. Sun, K. Liu, and H. Lei, Phys. Rev. Lett. **127**, 207002 (2021).

[51] H. Tan, Y. Liu, Z. Wang, and B. Yan, Phys. Rev. Lett. **127**, 046401 (2021).

[52] N. Shumiya, Md. S. Hossain, J.-X. Yin, Y.-X. Jiang, B. R. Ortiz, H. Liu, Y. Shi, Q. Yin, H. Lei, S. S. Zhang, G. Chang, Q. Zhang, T. A. Cochran, D. Multer, M. Litskevich, Z.-J. Cheng, X. P. Yang, Z. Guguchia, S. D. Wilson, and M. Z. Hasan, Phys. Rev. B **104**, 035131 (2021).

[53] F. H. Yu, D. H. Ma, W. Z. Zhuo, S. Q. Liu, X. K. Wen, B. Lei, J. J. Ying, and X. H. Chen, Nat. Commun. **12**, 3645 (2021).

[54] L. Yin, D. Zhang, C. Chen, G. Ye, F. Yu, B. R. Ortiz, S. Luo, W. Duan, H. Su, J. Ying, S. D. Wilson, X. Chen, H. Yuan, Y. Song, and X. Lu, Phys. Rev. B **104**, 174507 (2021).

[55] K. Nakayama, Y. Li, T. Kato, M. Liu, Z. Wang, T. Takahashi, Y. Yao, and T. Sato, Phys. Rev. B **104**, L161112 (2021).

[56] K. Jiang, T. Wu, J.-X. Yin, Z. Wang, M. Z. Hasan, S. D. Wilson, X. Chen, and J. Hu, Natl. Sci. Rev. **10**, nwac199 (2023).

[57] L. Nie, K. Sun, W. Ma, D. Song, L. Zheng, Z. Liang, P. Wu, F. Yu, J. Li, M. Shan, D. Zhao, S. Li, B. Kang, Z. Wu, Y. Zhou, K. Liu, Z. Xiang, J. Ying, Z. Wang, T. Wu, and X. Chen, Nature (London) **604**, 59 (2022).

[58] H. Luo, Q. Gao, H. Liu, Y. Gu, D. Wu, C. Yi, J. Jia, S. Wu, X. Luo, Y. Xu, L. Zhao, Q. Wang, H. Mao, G. Liu, Z. Zhu, Y. Shi, K. Jiang, J. Hu, Z. Xu, and X. J. Zhou, Nat. Commun. **13**, 273 (2022).

[59] T. Neupert, M. M. Denner, J.-X. Yin, R. Thomale, and M. Z. Hasan, Nat. Phys. **18**, 137 (2022).

[60] Y. Song, T. Ying, X. Chen, X. Han, X. Wu, A. P. Schnyder, Y. Huang, J.-G. Guo, and X. Chen, Phys. Rev. Lett. **127**, 237001 (2021).

[61] K. Nakayama, Y. Li, T. Kato, M. Liu, Z. Wang, T. Takahashi, Y. Yao, and T. Sato, Phys. Rev. X **12**, 011001 (2022).

[62] H. Li, H. Zhao, B. R. Ortiz, Y. Oey, Z. Wang, S. D. Wilson, and I. Zeljkovic, Nat. Phys. **19**, 637 (2023).

[63] C. Guo, C. Putzke, S. Konyzheva, X. Huang, M. Gutierrez-Amigo, I. Errea, D. Chen, M. G. Vergniory, C. Felser, M. H. Fischer, T. Neupert, and P. J. W. Moll, Nature (London) **611**, 461 (2022).

[64] H. Li, T. T. Zhang, T. Yilmaz, Y. Y. Pai, C. E. Marvinney, A. Said, Q. W. Yin, C. S. Gong, Z. J. Tu, E. Vescovo, C. S. Nelson, R. G. Moore, S. Murakami, H. C. Lei, H. N. Lee, B. J. Lawrie, and H. Miao, Phys. Rev. X **11**, 031050 (2021).

[65] H. Li, S. Wan, H. Li, Q. Li, Q. Gu, H. Yang, Y. Li, Z. Wang, Y. Yao, and H.-H. Wen, Phys. Rev. B **105**, 045102 (2022).

[66] X. Wu, T. Schwemmer, T. Müller, A. Consiglio, G. Sangiovanni, D. Di Sante, Y. Iqbal, W. Hanke, A. P. Schnyder, M. M. Denner, M. H. Fischer, T. Neupert, and R. Thomale, Phys. Rev. Lett. **127**, 177001 (2021).

[67] M. M. Denner, R. Thomale, and T. Neupert, Phys. Rev. Lett. **127**, 217601 (2021).

[68] S. Cho, H. Ma, W. Xia, Y. Yang, Z. Liu, Z. Huang, Z. Jiang, X. Lu, J. Liu, Z. Liu, J. Li, J. Wang, Y. Liu, J. Jia, Y. Guo, J. Liu, and D. Shen, Phys. Rev. Lett. **127**, 236401 (2021).

[69] Y.-P. Lin and R. M. Nandkishore, Phys. Rev. B **106**, L060507 (2022).

[70] L. Zheng, Z. Wu, Y. Yang, L. Nie, M. Shan, K. Sun, D. Song, F. Yu, J. Li, D. Zhao, S. Li, B. Kang, Y. Zhou, K. Liu, Z. Xiang, J. Ying, Z. Wang, T. Wu, and X. Chen, Nature (London) **611**, 682 (2022).

[71] C. Wen, X. Zhu, Z. Xiao, N. Hao, R. Mondaini, H.-M. Guo, and S. Feng, Phys. Rev. B **105**, 075118 (2022).

[72] R. Tazai, Y. Yamakawa, S. Onari, and H. Kontani, Sci. Adv. **8**, eabl4108 (2022).

[73] H.-M. Jiang, S.-L. Yu, and X.-Y. Pan, Phys. Rev. B **106**, 014501 (2022).

[74] C. Mielke III, D. Das, J.-X. Yin, H. Liu, R. Gupta, Y.-X. Jiang, M. Medarde, X. Wu, H. C. Lei, J. Chang, P. Dai, Q. Si, H. Miao, R. Thomale, T. Neupert, Y. Shi, R. Khasanov, M. Z. Hasan, H. Luetkens, and Z. Guguchia, Nature (London) **602**, 245 (2022).

[75] H. D. Scammell, J. Ingham, T. Li, and O. P. Sushkov, Nat. Commun. **14**, 605 (2023).

[76] F. Grandi, A. Consiglio, M. A. Sentef, R. Thomale, and D. M. Kennes, Phys. Rev. B **107**, 155131 (2023).
[77] B. R. Ortiz, L. C. Gomes, J. R. Morey, M. Winiarski, M. Bordelon, J. S. Mangum, I. W. H. Oswald, J. A. Rodriguez-Rivera, J. R. Neilson, S. D. Wilson, E. Ertekin, T. M. McQueen, and E. S. Toberer, Phys. Rev. Mater. **3**, 094407 (2019).
[78] E. M. Kenney, B. R. Ortiz, C. Wang, S. D. Wilson, and M. J. Graf, J. Phys.: Condens. Matter **33**, 235801 (2021).
[79] Y. Xu, Z. Ni, Y. Liu, B. R. Ortiz, Q. Deng, S. D. Wilson, B. Yan, L. Balents, and L. Wu, Nat. Phys. **18**, 1470 (2022).
[80] D. R. Saykin, C. Farhang, E. D. Kountz, D. Chen, B. R. Ortiz, C. Shekhar, C. Felser, S. D. Wilson, R. Thomale, J. Xia, and A. Kapitulnik, Phys. Rev. Lett. **131**, 016901 (2023).
[81] H. Li, H. Zhao, B. R. Ortiz, T. Park, M. Ye, L. Balents, Z. Wang, S. D. Wilson, and I. Zeljkovic, Nat. Phys. **18**, 265 (2022).
[82] C. Guo, G. Wagner, C. Putzke, D. Chen, K. Wang, L. Zhang, M. Gutierrez-Amigo, I. Errea, M. G. Vergniory, C. Felser, M. H. Fischer, T. Neupert, and P. J. W. Moll, Nat. Phys. (2024), arXiv:2304.00972.
[83] L. Yu, C. Wang, Y. Zhang, M. Sander, S. Ni, Z. Lu, S. Ma, Z. Wang, Z. Zhao, H. Chen, K. Jiang, Y. Zhang, H. Yang, F. Zhou, X. Dong, S. L. Johnson, M. J. Graf, J. Hu, H.-J. Gao, and Z. Zhao, arXiv:2107.10714.
[84] X. Zhou, H. Liu, W. Wu, K. Jiang, Y. Shi, Z. Li, Y. Sui, J. Hu, and J. Luo, Phys. Rev. B **105**, 205104 (2022).
[85] D. Chen, B. He, M. Yao, Y. Pan, H. Lin, W. Schnelle, Y. Sun, J. Gooth, L. Taillefer, and C. Felser, Phys. Rev. B **105**, L201109 (2022).
[86] Y. Hu, S. Yamane, G. Mattoni, K. Yada, K. Obata, Y. Li, Y. Yao, Z. Wang, J. Wang, C. Farhang, J. Xia, Y. Maeno, and S. Yonezawa, arXiv:2208.08036.
[87] X. Feng, K. Jiang, Z. Wang, and J. Hu, Sci. Bull. **66**, 1384 (2021).
[88] X. Feng, Y. Zhang, K. Jiang, and J. Hu, Phys. Rev. B **104**, 165136 (2021).
[89] J.-W. Dong, Z. Wang, and S. Zhou, Phys. Rev. B **107**, 045127 (2023).
[90] Z. Jiang, H. Ma, W. Xia, Q. Xiao, Z. Liu, Z. Liu, Y. Yang, J. Ding, Z. Huang, J. Liu, Y. Qiao, J. Liu, Y. Peng, S. Cho, Y. Guo, J. Liu, and D. Shen, Nano Lett. **23**, 5625 (2023).
[91] P. Wu, Y. Tu, Z. Wang, S. Yu, H. Li, W. Ma, Z. Liang, Y. Zhang, X. Zhang, Z. Li, Y. Yang, Z. Qiao, J. Ying, T. Wu, L. Shan, Z. Xiang, Z. Wang, and X. Chen, Nat. Phys. **19**, 1143 (2023).
[92] Q. Wu, Z. X. Wang, Q. M. Liu, R. S. Li, S. X. Xu, Q. W. Yin, C. S. Gong, Z. J. Tu, H. C. Lei, T. Dong, and N. L. Wang, Phys. Rev. B **106**, 205109 (2022).
[93] Y. Zhong, J. Liu, X. Wu, Z. Guguchia, J.-X. Yin, A. Mine, Y. Li, S. Najafzadeh, D. Das, C. Mielke III, R. Khasanov, H. Luetkens, T. Suzuki, K. Liu, X. Han, T. Kondo, J. Hu, S. Shin, Z. Wang, X. Shi, Y. Yao, and K. Okazaki, Nature (London) **617**, 488 (2023).
[94] Y. Gu, Y. Zhang, X. Feng, K. Jiang, and J. Hu, Phys. Rev. B **105**, L100502 (2022).
[95] H.-M. Jiang, M.-X. Liu, and S.-L. Yu, Phys. Rev. B **107**, 064506 (2023).
[96] T. Park, M. Ye, and L. Balents, Phys. Rev. B **104**, 035142 (2021).
[97] J. Zhao, W. Wu, Y. Wang, and S. A. Yang, Phys. Rev. B **103**, L241117 (2021).
[98] Y. Li, Q. Li, X. Fan, J. Liu, Q. Feng, M. Liu, C. Wang, J.-X. Yin, J. Duan, X. Li, Z. Wang, H.-H. Wen, and Y. Yao, Phys. Rev. B **105**, L180507 (2022).
[99] M. H. Christensen, T. Birol, B. M. Andersen, and R. M. Fernandes, Phys. Rev. B **104**, 214513 (2021).
[100] R. Nandkishore, L. S. Levitov, and A. V. Chubukov, Nat. Phys. **8**, 158 (2012).
[101] Y.-P. Lin and R. M. Nandkishore, Phys. Rev. B **100**, 085136 (2019).
[102] Y.-P. Lin and R. M. Nandkishore, Phys. Rev. B **104**, 045122 (2021).
[103] G. Liu, X. Ma, K. He, Q. Li, H. Tan, Y. Liu, J. Xu, W. Tang, K. Watanabe, T. Taniguchi, L. Gao, Y. Dai, H.-H. Wen, B. Yan, and X. Xi, Nat. Commun. **13**, 3461 (2022).
[104] Y. Xie, Y. Li, P. Bourges, A. Ivanov, Z. Ye, J.-X. Yin, M. Z. Hasan, A. Luo, Y. Yao, Z. Wang, G. Xu, and P. Dai, Phys. Rev. B **105**, L140501 (2022).
[105] C. Wang, S. Liu, H. Jeon, Y. Jia, and J.-H. Cho, Phys. Rev. Mater. **6**, 094801 (2022).
[106] M. Gutierrez-Amigo, D. Dangić, C. Guo, C. Felser, P. J. W. Moll, M. G. Vergniory, and I. Errea, arXiv:2311.14112.